The Astrophysical Journal, 700:977–988, 2009 August 1 doi:10.1088/0004-637X/700/2/977

THE PHOTOIONIZED ACCRETION DISK IN HER X-1

L. Ji[1], N. Schulz[1], M. Nowak[1], H. L. Marshall[1], and T. Kallman[2]
[1] MIT Kavli Institute for Astrophysics and Space Research, Cambridge, MA, USA; ji@space.mit.edu
[2] NASA Goddard Space Flight Center, NASA, Greenbelt, MD, USA
Received 2009 January 12; accepted 2009 May 25; published 2009 July 7

ABSTRACT

We present an analysis of several high-resolution *Chandra* grating observations of the X-ray binary pulsar Her X-1. With a total exposure of 170 ks, the observations are separated by years and cover three combinations of orbital and superorbital phases. Our goal is to determine distinct properties of the photoionized emission and its dependence on phase-dependent variations of the continuum. We find that the continua can be described by a partial covering model which above 2 keV is consistent with recent results from *Rossi X-Ray Timing Explorer* studies and at low energies is consistent with recent *XMM-Newton* and *BeppoSAX* studies. Besides a power law with fixed index, an additional thermal blackbody of 114 eV is required to fit wavelengths above 12 Å (∼1 keV). We find that likely all the variability is caused by highly variable absorption columns in the range $(1–3) \times 10^{23}$ cm^{-2}. Strong Fe K line fluorescence in almost all observations reveals that dense, cool material is present not only in the outer regions of the disk but interspersed throughout the disk. Most spectra show strong line emission stemming from a photoionized accretion disk corona (ADC). We model the line emission with generic thermal plasma models as well as with the photoionization code XSTAR and investigate changes of the ionization balance with orbital and superorbital phases. Most accretion disk coronal properties such as disk radii, temperatures, and plasma densities are consistent with previous findings for the low state. We find that these properties change negligibly with respect to orbital and superorbital phases. A couple of the higher energy lines exhibit emissivities that are significantly in excess of expectations from a static ADC.

Key words: accretion, accretion disks – binaries: eclipsing – line: formation – line: identification – pulsars: individual (Hercules X-1) – X-rays: binaries

Online-only material: color figures

1. INTRODUCTION

The mechanisms involved in accretion processes of X-ray binaries are still quite poorly understood specifically when it comes to feedback effects and how they affect the overall X-ray luminosity. In low-mass X-ray binaries (LMXBs), a neutron star or a stellar black hole accretes matter from its companion entirely via Roche-lobe overflow and a steady accretion disk is formed. The bulk of the gravitational energy is released in the form of X-rays near the compact object at luminosities of up to over 10^{38} erg s^{-1}. LMXBs have been classified into two major categories based on their correlated spectral and timing behavior into Z- and atoll sources, where the former predominantly radiate near their Eddington luminosities, the latter radiate generally an order of magnitude lower (Hasinger & van der Klis 1989; Schulz et al. 1989).

Although Her X-1 (Tananbaum et al. 1972) is not a typical LMXB, its bulk mass accretion also comes from Roche-lobe overflow and it possesses a sizeable accretion disk. With respect to the Atoll and Z-source classification scheme, Her X-1 has been associated with neither. However, properties of accretion disk coronae (ADCs), as observed in some Atoll sources viewed at high inclination angles such as 4U 1822-37 (Cottam et al. 2001), 2S 0921-63 (Kallman et al. 2003), or EXO 0748-767 (Jimenez-Garate et al. 2003), have also been observed in Her X-1 (Jimenez-Garate et al. 2005). From the point of accretion dynamics (i.e., the structures of the outer accretion disk), we expect Her X-1 to behave very much like these Atoll sources. There are two primary differences with respect to LMXBs in the Her X-1 system besides the larger companion mass of $2.3 \pm 0.3\ M_{\odot}$. One is a high magnetic field of the accreting neutron star leading to the 1.24 s X-ray pulsation period and therefore some fraction of its X-rays come from the polar cap accretion columns. LMXBs have lower magnetic fields and most of them likely lack this component in their emissions although 4U 1822-37 has a detected X-ray pulse with a period of 0.59 s (Jonker & van der Klis 2001). Her X-1, besides its orbital period of $P_{\rm orb} = 1.7$ days, also possesses a $P_{\Psi} \sim 35$ day superorbital period likely due to some form of disk warp. Such periods have also been observed in systems with high-mass companions (HMXBs) such as LMC X-4 and SMC X-1. Evidence that a stellar wind is affecting the observability of disk signatures in the ultraviolet (UV) has been presented recently (Boroson et al. 2007). Either accretion disk winds (Schandl & Mayer 1994) or radiation pressure effects (Maloney & Begelman 1997) are considered to cause this precessing warp.

Emissions from accretion in X-ray binaries are observed from about several eV up to hundreds of keV. Each energy band carries information about specific emission processes, the nature of the radiative source itself, as well as its location. In rough terms it goes like the following scheme. Optical emission is usually associated with the companion star HZ Her which is indirectly affected by heating from the X-ray source (Middleditch & Nelson 1976; Still et al. 1997). The latter primarily manifests itself in the UV which also hosts the bulk of the continuum emission from the accretion disk. UV emission lines, the strongest include C IV, N V, Si IV, result from photoionization of large portions of the accretion disk (Howard & Wilson 1983; Cheng et al. 1995; Raymond 1993; Ko & Kallman 1994). In his classic and comprehensive model of an X-ray-illuminated surface of the accretion disk in LMXBs, Raymond (1993) produced UV lines consistent with

Table 1
Observations for Her X-1

obsID	MJD Interval	Obs. Start	Exp. (ks)	$\theta_{\rm Orb.}$[a]	Ψ_{35d}[a]
2749	52399.427−52400.032	2002-05-05 10:14:49 UT	50.17	0.33–0.68	0.42
3821	52875.886−52876.261	2003-08-24 21:15:16 UT	30.10	0.57–0.79	−0.03
3822	52982.987−52983.379	2003-12-09 23:41:44 UT	30.14	0.57–0.80	0.04
4585	53335.256−53335.512	2004-11-26 06:08:16 UT	20.16	0.76–0.91	0.10
6149	53338.630−53338.913	2004-11-29 15:06:38 UT	22.14	0.75–0.91	0.19
6150	53340.370−53340.647	2004-12-01 08:52:39 UT	22.05	0.77–0.93	0.24

Note.
[a] Using $P_{\rm orb} = 1.700167387$ d at $T_{\pi/2} = 50290.659202$ (MJD) (R. Staubert 2007, private communication).

observations in LMXBs and Her X-1 as well as predicted soft X-ray line emission on top of the blackbody emission from the inner disk (Oosterbroek et al. 2001). Most of the hard X-rays above 10–20 keV come from the central source in form of Compton scattering of thermal emission from the central source as well as synchrotron emission from the accretion column. The discovery of a 42 keV synchrotron line allowed a magnetic field determination of 3.5×10^{12} G (Trümper et al. 1978; dal Fiume et al. 1998). A recent account of X-ray emissions observed with *RXTE* can be found in Kuster et al. (2005).

In this paper, we concentrate on X-ray properties in the 0.1–8 keV band with emphasis on orbital and superorbital influence on photoionized properties of the accretion disk. *BeppoSAX* observations obtained during the main-on state described a spectral continuum consisting of a power law of index 0.74 and a strong 0.093 keV blackbody component plus a broad Fe L line complex at 0.937 keV and an Fe K line complex at 6.4 keV (Oosterbroek et al. 2001). More recently, multiple *RXTE* observations scanned the turn-on, a transition from the low state to the main-on state in the 35 day cycle, and found an evolution in the spectral continuum dominated by scattering and partial covering absorption (Kuster et al. 2005). In a first high-resolution pilot study, Jimenez-Garate et al. (2005) identified an extended ADC in Her X-1's low state using high-resolution X-ray spectra from *Chandra*. More than two dozen recombination lines from Fe XXVI (1.78 Å) to N VI (29.08 Å) were detected and emission radii between 8×10^{10} and 1×10^{11} cm were derived. Line optical depth diagnostics were consistent with a flattened atmosphere. These properties were derived for the low state and the question remains how they change with respect to orbital and superorbital phase. The pilot study also deduced an overabundance of nitrogen relative to the other metals, which had been predicted from UV line studies.

The following analysis covers half a dozen exposures of Her X-1 with the High Energy Transition Grating Spectrometer (HETGS) onboard *Chandra* (Canizares et al. 2005) including the one presented by Jimenez-Garate et al. (2005). In Section 2, we present the observations, light curves, and continuum fits. Sections 3–5 cover line detections, emission measures (EMs), and the discussion of their implications, respectively.

2. *CHANDRA* OBSERVATIONS

The *Chandra* archive to date includes a total of six HETGS observations of Her X-1 that were performed in the timed event (TE) mode. The basic observation statuses are summarized in Table 1. These observations span several different phase combinations with respect to orbital and superorbital phase, the low state (OBSID 2749), the turn-on (OBSIDs 3821, 3822), the main-on (OBSIDs 4585, 6149), and the turn-off (OBSID 6150). We reprocess all the observations using CIAO Version 4.1 with the most recent CALDB products. We restrict the analysis to observations obtained in the TE mode to maintain the most coherent calibration status. Some observations in the archive were taken in continuous clocking mode during a specifically bright episode of the source. Here we opt to wait for better calibration in order to relate the CC mode data to the TE mode data.

For each observation, we then re-determine the positions of the zeroth-order centroid for optimal wavelength accuracy. We extract all first-order spectra in HEG and MEG and combine them. Light curves and spectral analysis are based on ISIS Version 1.4.7 (Houck & Denicola 2000).

2.1. Light Curve Analysis

In order to generate a long-term average X-ray light curve, we use all the observations obtained from the All-Sky Monitor (ASM) instrument on board the *Rossi X-Ray Timing Explorer* (*RXTE*). The left panel in Figure 1 shows this light curve and highlights the phase locations for all *Chandra* observations from Table 1. We show the light curve for two orbital reference phases. We superpose all 35 day light curves corresponding to cycles with turn-ons near orbital phase of about 0.2 s (right panel, similar for 0.7 s orbital phase). The 35 day phase ephemeris was provided by R. Staubert (2007, private communication; Staubert et al. 2007).

The HETGS light curves were integrated in bins of 100 s and for wavelengths with $\lambda > 1.5$ Å (Figure 2). Count rates vary from about 0.2–30 counts s^{-1}. OBSID 2749 is in the off state, OBSID 6150 is close to the off state, and flux variations are small in both. There are some small flares in the turn-on state (OBSIDs 3821 and 3822). Dramatic flux variations by almost 2 orders of magnitude occur in the main-on observations in OBSIDs 4585 and 6149.

Significant flux variations indicate the existence of various substates within single observations. We separate the two observations during main-on into high and low flux substates as well as recognized dipping phases. For the dipping phase during the main-on, we further examine the color–color diagrams and separate main-high, main-dip, and main-low phases. The left and middle panels of Figure 3 show the separated regions marked in the light curve of OBSIDs 4585 and 6149, respectively. The right panel of Figure 3 illustrates their positions in the color–color diagram for the main-on stage. We compute the count rates from three wavelength bands: a low band [5, 25] Å, a middle band [2.8, 5.0] Å, and a high band [1.0, 2.8] Å for each light curve and calculate count rate ratios. The soft color is the ratio of the middle to the high wavelength band, the hard color ratio is the ratio of the low to the middle wavelength band.

The main-high substate exhibits the lowest soft and hard ratios, with values accumulating in the lower left corner of the color–color diagram. The main-dip remains at low hard

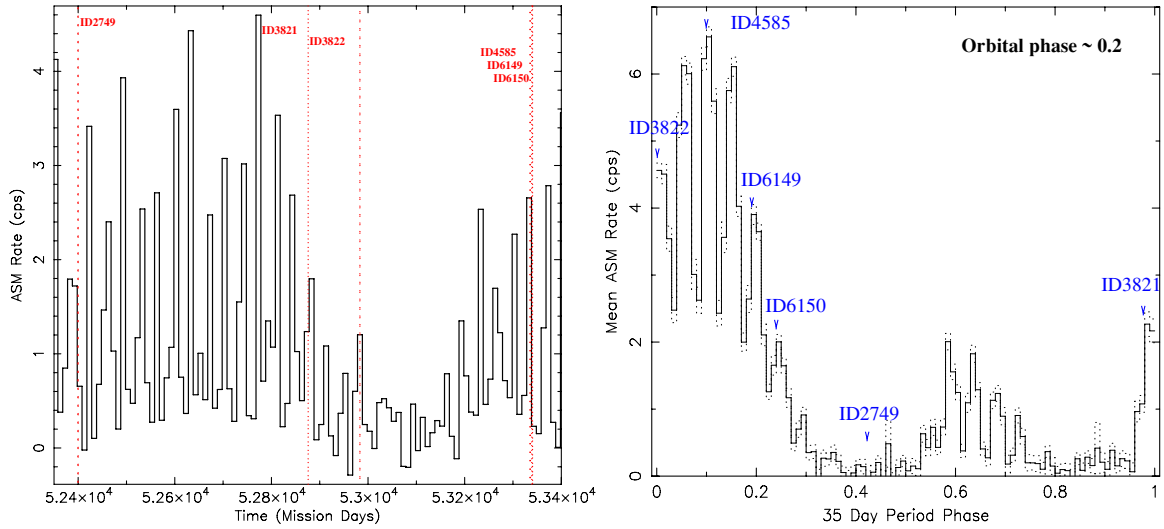

Figure 1. Left: Her X-1 ASM light curve; right: averaged X-ray light curves of Her X-1 corresponding to cycles with turn-ons near orbital phase ∼0.2.
(A color version of this figure is available in the online journal.)

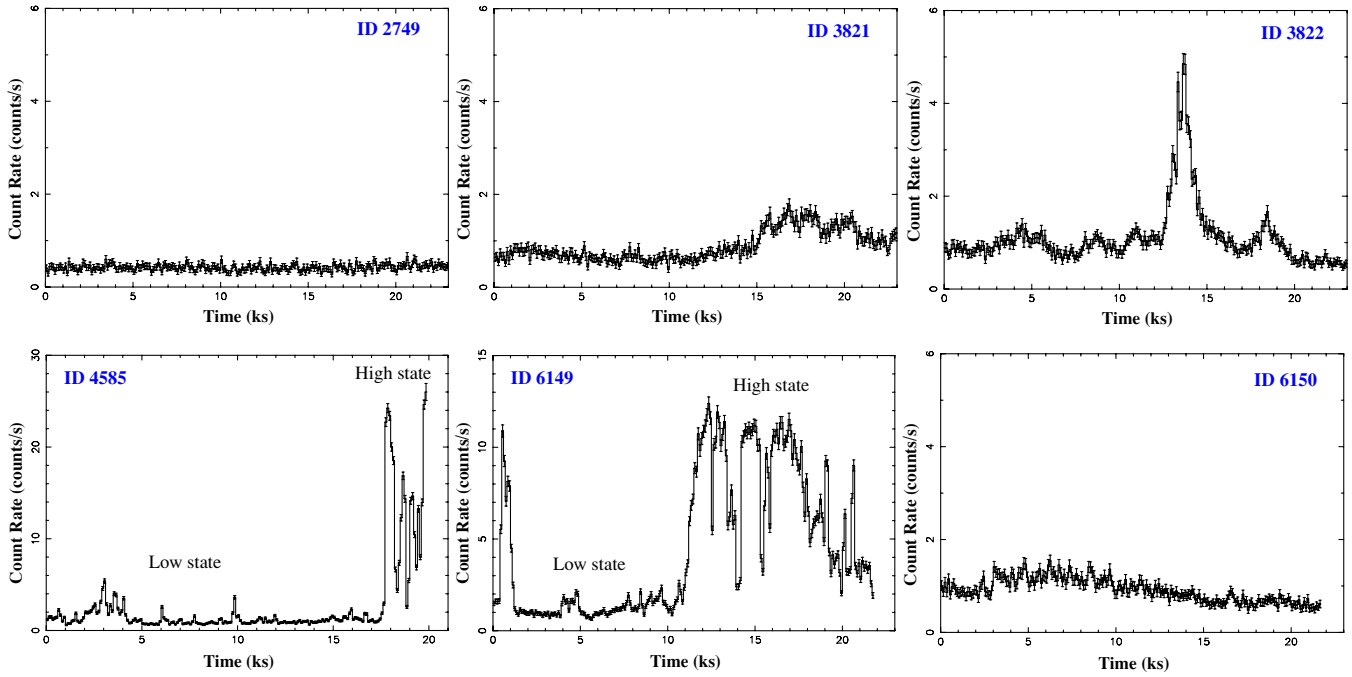

Figure 2. Light curve for all phases with $\lambda > 1.5$ Å.
(A color version of this figure is available in the online journal.)

ratios, but expands to higher soft ratios. In contrast, the main-low substate remains mostly at low soft ratios but expands to higher hard ratios. In that respect, dip and low states during the main-on phase appear to be qualitatively different in their spectral evolution. Thus, although the color–color diagram on the whole appears not very well structured, mostly due to a somewhat erratic behavior during the low states, these spectral variations do not appear atypical for atoll sources.

2.2. Continuum Analysis

Generally continuum modeling involves two components: absorbers and emitters. Recent studies established power-law and blackbody functions to model the continuum in the Her X-1 (see Oosterbroek et al. 2001). Besides low foreground neutral absorption due to the interstellar medium (ISM), additional neutral and ionized absorbers have been applied to fit the continuum during the dips (Díaz Trigo et al. 2006). Other authors favor a partial covering model (Brandt et al. 1996; Kuster et al. 2005). Spectral changes in the different phases of Her X-1 seem to require at least the latter (Kuster et al. 2005).

Following that analysis, we model the spectrum of the emitting source with a power law and a high-energy exponential cutoff. Based on those *RXTE* observations of the turn-on phase of a 35 day cycle of Her X-1, this continuum plus a partial covering model can well describe the high-energy spectra in the [3, 17] keV range. To be consistent with the *RXTE* studies, we fix the power-law photon index at 1.068 and the high-energy cutoff at 21.5 keV in all fits.

Located at high Galactic latitude, Her X-1 suffers from very small reddening. Photoelectric absorption from the line-of-sight

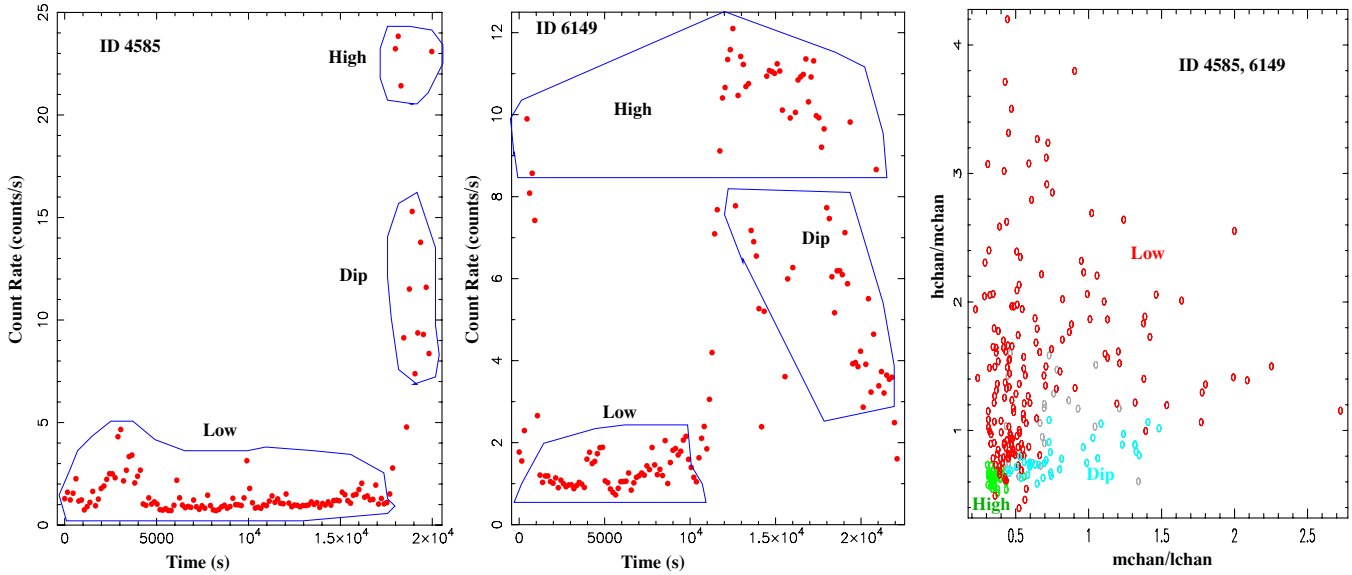

Figure 3. Light curves for ID 4585 (left), ID 6149 (middle): separated into three regions (High, Low, and Dip). Right panel: color–color diagram for ID 4585, 6149, High (green), Low (red), Dip (cyan). Note: lchan:[5, 25] Å, mchan:[2.8, 5.0] Å, hchan:[1.0, 2.8] Å. See the text for details.

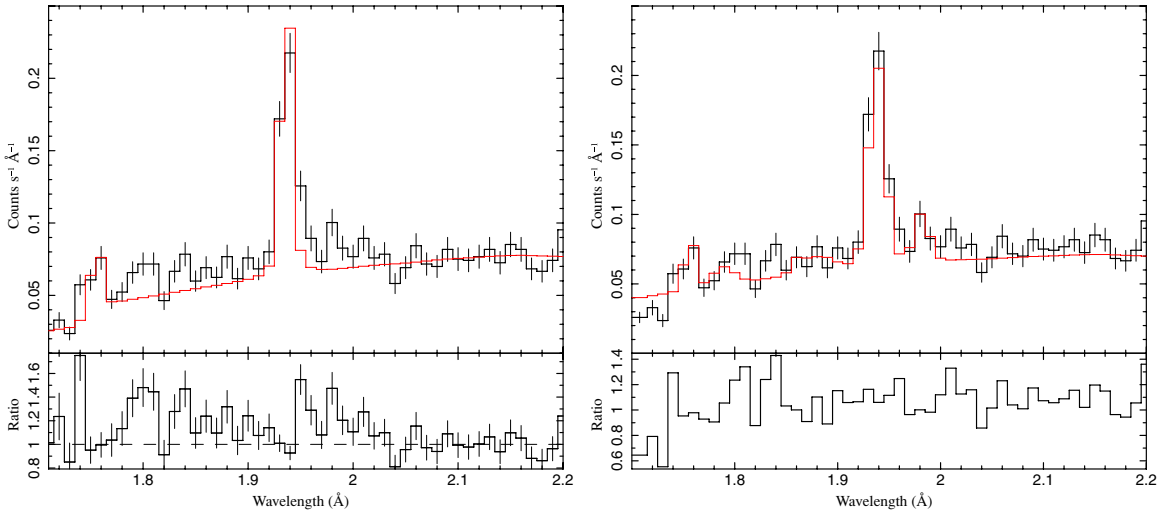

Figure 4. ID 3822: with (left) and without (right) local absorption.

ISM is fixed at $N_H = 1.3 \times 10^{18}$ cm^{-2} (Jimenez-Garate et al. 2005). We detected significant optical depth at the Fe K edges in all the observations indicating that significant amounts of absorption exist locally. A partial covering fraction absorption function matches well to these Fe K edges which is illustrated in Figure 4.

All HETG fits also showed significant residuals above 12 Å (below 1 keV) requiring an additional component. This is illustrated in Figure 5. A thermal blackbody of 114 eV consistently fit the residuals in all cases.

The best-fit results for all phases are summarized in Table 2. All phases exhibit substantial local absorption on the order of 10^{23} cm^{-2} at large covering fractions, which indicates a large fraction of local cold material blocking our line of sight, even during the main-on maximum state OBSID 4585. In addition, we find that the higher the column density, the higher the partial covering factors are. The column density of the low, on, or off stage is more than 1 mag larger than the one in the high or dipper stage. This is consistent with the superorbital phase since main high (or dipper) stage suffers less blocking from the central X-ray emitter or the local absorbers, which is confirmed by a smaller covering factor and lower column density. Due to the high inclination of the system ($i > 80$), such local absorption is likely due to the accretion disk.

Table 3 presents the best continuum fitting results according to the different stages and substages. The implications are the same as those for Table 2. Therefore, for the lines from Sections 3 to 5, we make our analysis based on the continuum presented in Table 2. We also apply the "tbnew" model[3] (Wilms et al. 2000) which has updated absorption cross sections to replace the phabs model, resulting in roughly twice the values of the fitted N_H.

The size of the thermal region can be derived from the flux of the thermal blackbody component according to $L = \sigma T^4 4\pi R^2$: R (km) $= 0.18361\sqrt{K(10^{-5})}/T^2$(keV), where K is the normalization of the blackbody in units of 10^{34} erg s^{-1}/(10 kpc)^2. The size of the thermal component then varies from about 10 km to 100 km, indicating the emission does not

[3] http://pulsar.sternwarte.uni-erlangen.de/wilms/research/tbabs/

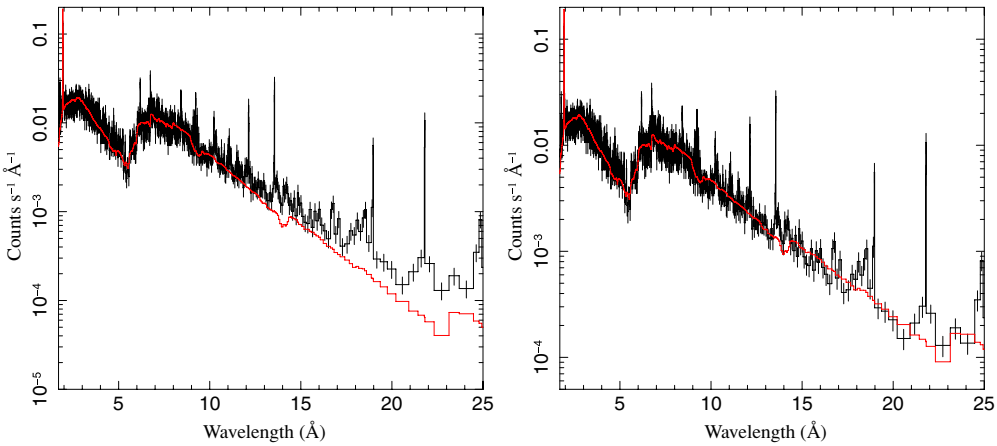

Figure 5. ID 2749: with (right) and without (left) blackbody component.
(A color version of this figure is available in the online journal.)

Table 2
Continuum Fits for Her X-1 Using pcfabs(bbody+cutoffpl)

obsID	nH (10^{22} cm^{-2})	f_{pc}	kT (keV)	K1[a] (10^{39} erg s^{-1}/(10 kpc)^2)	K2[b] (photons keV^{-1} cm^{-2} s^{-1})	χ^2/d.o.f.	Flux[d]	Lumi[e]
2749	$19.6^{+1.6\,c}_{-1.5}$	$0.753^{+0.020}_{-0.018}$	$0.129^{+0.012}_{-0.012}$	$1.3^{+0.4}_{-0.3}\times10^{-4}$	$7.4^{+0.7}_{-0.6}\times10^{-3}$	1026/598	0.4	0.5
3821	$19.3^{+1.4}_{-1.3}$	$0.833^{+0.008}_{-0.009}$	$0.100^{+0.014}_{-0.013}$	$4.8^{+2.7}_{-1.6}\times10^{-4}$	$3.1^{+0.2}_{-0.2}\times10^{-2}$	1068/781	1.0	1.9
3822	$28.3^{+1.7}_{-1.4}$	$0.907^{+0.005}_{-0.005}$	>0.052	$>3.3\times10^{-4}$	$4.4^{+0.3}_{-0.2}\times10^{-2}$	970/673	0.7	2.8
4585-H	$11.3^{+1.2}_{-1.1}$	$0.734^{+0.012}_{-0.012}$	$0.141^{+0.008}_{-0.008}$	$3.5^{+0.5}_{-0.4}\times10^{-3}$	$1.4^{+0.1}_{-0.1}\times10^{-1}$	977/795	9.9	9.7
6149-H	$10.3^{+1.0}_{-0.6}$	$0.699^{+0.004}_{-0.007}$	$0.136^{+0.003}_{-0.004}$	$3.1^{+0.3}_{-0.2}\times10^{-3}$	$9.4^{+0.3}_{-0.2}\times10^{-2}$	1665/1208	8.8	6.6
4585-L	$30.0^{+0.8}_{-0.8}$	0.95	$0.110^{+0.015}_{-0.016}$	$1.7^{+1.1}_{-0.6}\times10^{-3}$	$7.9^{+0.2}_{-0.2}\times10^{-2}$	664/454	0.9	5.2
6149-L	$24.6^{+1.5\,c}_{-1.4}$	$0.884^{+0.010}_{-0.010}$	$0.127^{+0.014}_{-0.013}$	$1.2^{+0.4}_{-0.3}\times10^{-3}$	$5.8^{+0.5}_{-0.5}\times10^{-2}$	520/426	1.6	3.8
6150	$27.7^{+2.3}_{-1.9}$	$0.897^{+0.008}_{-0.007}$	$0.110^{+0.014}_{-0.013}$	$6.4^{+3.0}_{-2.0}\times10^{-4}$	$3.6^{+0.3}_{-0.2}\times10^{-2}$	782/530	0.8	2.3

Notes.
[a] Normalization for blackbody component.
[b] Normalization for cutoff power-law component, where photon index is fixed at 1.068 and high-energy cut at 21.5 keV.
[c] At 67% confidence level.
[d] Detected flux is in unit of 10^{-11} erg s^{-1} cm^{-2} and in [0.3,10] keV band.
[e] Absorption-corrected luminosity is in unit of 10^{36} erg s^{-1} and in [0.3,10] keV band.

Table 3
Continuum Fits for Her X-1 Using pcfabs(bbody+cutoffpl)

Stage	obsID	nH (10^{22} cm^{-2})	f_{pc}	kT (keV)	K1[a] (10^{39} erg s^{-1}/(10 kpc)^2)	K2[b] (photons keV^{-1} cm^{-2} s^{-1})	χ^2/d.o.f.
Low	2749	$19.6^{+1.6\,c}_{-1.5}$	$0.753^{+0.020}_{-0.018}$	$0.129^{+0.012}_{-0.012}$	$1.3^{+0.4}_{-0.3}\times10^{-4}$	$7.4^{+0.7}_{-0.6}\times10^{-3}$	1026/598
Turn-on	3821	$19.3^{+1.4}_{-1.3}$	$0.833^{+0.008}_{-0.009}$	$0.100^{+0.014}_{-0.013}$	$4.8^{+2.7}_{-1.6}\times10^{-4}$	$3.1^{+0.2}_{-0.2}\times10^{-2}$	1068/781
Turn-on	3822	$28.3^{+1.7}_{-1.4}$	$0.907^{+0.005}_{-0.005}$	> 0.052	$>3.3\times10^{-4}$	$4.4^{+0.3}_{-0.2}\times10^{-2}$	970/673
Main-high	4585,6149	$9.3^{+1.6}_{-0.8}$	$0.631^{+0.011}_{-0.007}$	$0.143^{+0.005}_{-0.004}$	$37.7^{+3.9}_{-2.5}\times10^{-4}$	$11.3^{+0.6}_{-0.3}\times10^{-2}$	1352/1052
Main-dip	4585,6149	$9.8^{+0.7}_{-0.7}$	$0.769^{+0.008}_{-0.008}$	$0.124^{+0.007}_{-0.007}$	$7.9^{+2.2}_{-2.2}\times10^{-4}$	$12.8^{+0.5}_{-0.5}\times10^{-2}$	1060/843
Main-low	4585,6149	$32.2^{+1.2}_{-1.2}$	$0.946^{+0.002}_{-0.003}$	$0.121^{+0.012}_{-0.011}$	$1.1^{+0.3}_{-0.3}\times10^{-3}$	$8.2^{+0.4}_{-0.4}\times10^{-2}$	1051/670
Turn-off	6150	$27.7^{+2.3}_{-1.9}$	$0.897^{+0.008}_{-0.007}$	$0.110^{+0.014}_{-0.013}$	$6.4^{+3.0}_{-2.0}\times10^{-4}$	$3.6^{+0.3}_{-0.2}\times10^{-2}$	782/530
Main-Ht	4585,6149	$15.3^{+2.0}_{-1.8}$	$0.640^{+0.007}_{-0.010}$	$0.143^{+0.004}_{-0.004}$	$38.6^{+2.6}_{-2.7}\times10^{-4}$	$11.6^{+0.5}_{-0.5}\times10^{-2}$	1350/1052
Main-Dt	4585,6149	$15.2^{+1.2}_{-1.1}$	$0.769^{+0.008}_{-0.008}$	$0.124^{+0.006}_{-0.005}$	$7.9^{+2.2}_{-2.2}\times10^{-4}$	$12.8^{+0.5}_{-0.4}\times10^{-2}$	1059/843
Main-Lt	4585,6149	$50.2^{+1.9}_{-1.9}$	$0.947^{+0.002}_{-0.002}$	$0.121^{+0.012}_{-0.011}$	$1.1^{+0.3}_{-0.3}\times10^{-3}$	$8.2^{+0.4}_{-0.4}\times10^{-2}$	1045/670

Notes.
[a] Normalization for blackbody component.
[b] Normalization for cutoff power-law component, where photon index is fixed at 1.068 and high-energy cut at 21.5 keV.
[c] At 67% confidence level.

Table 4
FeK$_\alpha$, FeK$_\beta$ for Her X-1 with pcfabs(bbody+cutoffpl)

obsID	λ_{K_α} (Å)	F (K$_\alpha$)[a] (10^{-4})	EW (K$_\alpha$) (eV)	$\sigma_{K_{\alpha,\beta}}$ (10^{-3} Å)	$R^b=\frac{F(K_\beta)}{F(K_\alpha)}$	Cash/d.o.f.	τ 0.1
2749	$1.938^{+0.001}_{-0.001}$	$4.1^{+0.4}_{-0.4}$	635^{+59}_{-57}	$2.8^{+1.2}_{-1.6}$	$0.16^{+0.07}_{-0.06}$	52/26	< 1.7
3821	$1.939^{+0.001}_{-0.002}$	$6.3^{+0.9}_{-0.9}$	243^{+34}_{-33}	$9.9^{+2.7}_{-2.3}$	$0.19^{+0.13}_{-0.12}$	63/28	$3.0^{+1.6}_{-1.5}$
3822	$1.938^{+0.001}_{-0.001}$	$8.8^{+1.0}_{-0.9}$	274^{+31}_{-29}	$7.5^{+1.6}_{-1.4}$	$0.38^{+0.12}_{-0.11}$	94/28	$5.7^{+1.6}_{-1.5}$
4585-H	...	...	...	...	...	...	...
6149-H	$1.940^{+0.001}_{-0.001}$	$6.3^{+1.2}_{-1.1}$	81^{+15}_{-14}	1.0	$0.24^{+0.22}_{-0.18}$	237/28	...
4585-L	1.94	$5.7^{+1.3}_{-1.2}$	116^{+26}_{-24}	1.0	$0.57^{+0.30}_{-0.23}$	226/29	$5.5^{+1.5}_{-1.4}$
6149-L	$1.940^{+0.001}_{-0.001}$	$9.8^{+1.9}_{-1.8}$	207^{+41}_{-37}	$7.5^{+2.7}_{-2.1}$	$0.23^{+0.21}_{-0.17}$	56/26	$5.7^{+2.6}_{-2.4}$
6150	$1.939^{+0.001}_{-0.002}$	$5.5^{+1.0}_{-0.9}$	209^{+37}_{-33}	$5.1^{+3.0}_{-2.9}$	$0.35^{+0.18}_{-0.15}$	76/28	$3.3^{+1.7}_{-1.6}$

Note.
[a] Its unit is photons s^{-1} cm^{-2}.

originate from the neutron star surface but likely favors an inner disk origin. Given a distance of 6.6 kpc, dal Fiume et al. (1998) measured a flux with *BeppoSAX* in the [0.1, 200] keV band of 7.2×10^{-9} erg s^{-1} cm^{-2}, corresponding to a total luminosity of about 3.8×10^{37} erg s^{-1}. Their observation was near the maximum of the 35 day X-ray intensity cycle. The luminosity of our detection for the main-on maximum state in OBSID 4585 is about 3.6×10^{37} erg s^{-1}, which is consistent with the *BeppoSAX* result.

Table 2 shows that luminosities in the [0.3, 10] keV band for all phases are within a factor of a few except the one in low state of OBSID 2749, which is almost 1 mag lower. Given stable accretion in Her X-1, the luminosity of the central source ought to be constant. How real these fluctuations are needs to be determined. It is interesting to note that these variations seem to correlate with observed flux and partial covering absorption, indicating that our model parameters for the partial coverage may provide an incomplete description. The same correlation may also mean that we see real variations in the heating of the ADC at different phases.

3. FLUORESCENCE LINE ANALYSIS

X-ray fluorescence probes physical conditions of cool circumstellar material in the vicinity of strong X-ray sources. X-ray emission from a hot, optically thin photoionized atmosphere occurs close to the illuminating X-ray source; in contrast, fluorescence from a cold, optically thick medium is effective at orders of magnitude larger distances. X-ray spectral properties of the Fe K region is extensively discussed in Kallman et al. (2004). We detect Fe K$_\alpha$ and Fe K$_\beta$ fluorescence lines at all phases except the high state of the main-on maximum phase (OBSID 4585). The fits were performed using the continuum solution from the analysis in Section 2, but with additional Gaussian line components. We assume that line broadening is the same for both Fe K$_\alpha$ and Fe K$_\beta$ lines. The relative wavelength position between Fe K$_\alpha$ and Fe K$_\beta$ was fixed in the way that the Fe K$_\beta$ wavelength scales by the theoretical K fluorescence wavelengths of the neutral iron Fe I (Kaastra & Mewe 1993).

The Fe K line region appears complex in almost all cases. Besides the line fluorescence we also observe hot lines from Fe XXV and Fe XXVI ions (see below). Specifically, the fits for the weaker Fe K$_\beta$ are problematic due to its proximity to the Fe K edge location at 1.74 Å as well as the Fe XXVI line location at 1.78 Å. Table 4 summarizes the observed values. The line centers of the Fe Kα line are consistent with 1.94 Å, which represent neutral Fe states between Fe I and Fe X. The lines appear resolved, the widths listed in Table 4 are significant. It is interesting to note that the values increase with measured line fluxes. Their equivalent Doppler widths range from 620 km s^{-1} in the turn-off to 2100 km s^{-1} in the turn-on.

The ratios of Fe K$_\beta$/K$_\alpha$ are generally larger than the theoretical value of 0.13 from Kaastra & Mewe (1993). More comparisons between various theoretical and experimental studies of this ratio are presented in Palmeri et al. (2003). This study shows that such a ratio could be as high as 0.17 for Fe IX. For our observations, during the turn-off and shortly after in the turn-on, the values are close to the 0.13 equilibrium value. In all other cases we observe values between 0.24 and 0.57, where the latter seems unrealistically high. We note that the error bars are all large for those high ratios. Excess Fe K$_\beta$ might be due to errors in fitting the Fe K edge. In order to match the Fe K edge, Fe K$_\beta$ could be overestimated. We have not been aware of any intrinsic atomic processes in the literature which could account for such higher ratios. We know that unlike Fe K$_\alpha$, Fe K$_\beta$ must come from the less ionized Fe ions (<Fe XVII) which have M shell electrons. The confusion from the higher ionized Fe ions can only lead to the larger production of Fe K$_\alpha$, which is clearly not the case here. Therefore, the known scenarios that possible extra contributions from the very hot inner portion of the disk or some highly illuminated layers of the companion star during the main-on, which all favor the larger production of Fe K$_\alpha$, could be excluded. Thus, we have no natural explanation for such a ratio.

Figure 6 shows the Fe K$_\alpha$ versus Fe K edge flux for all observations. The edge flux is defined as the continuum flux beyond the Fe K edge up to 1.55 Å (8.0 keV), which generally provides the bulk of the ionizing photons. Similar behavior between the Fe K$_\alpha$ versus Fe K edge flux has been presented by Makishima (1986) for a few Galactic X-ray binaries and extragalactic active galactic nuclei (AGNs). In Her X-1, as we approach the main-on, the Fe K$_\alpha$ line flux should increase as the continuum flux increases. Naturally, we would expect a monotonic increase of the Fe K$_\alpha$ line flux with edge flux. For most of the observations, this seems to be the case. However, this is not true for the two observations covering the main-on low flux state. Although here the edge flux appears twice to three times higher with respect to the other observations, the corresponding fluorescence line fluxes are not significantly higher. It is to note

Table 5
Line Flux[a] Detections for Her X-1

Lines	λ	*F* (Low State)	*F* (Main On)		*F* (Main High)		*F* (Main Low)		
	(Å)	2749	3821	3822	4585H	6149H	4585L	6149L	6150
S XVI Lyα	4.729	$4.4^{+2.0}_{-1.7}$	...	$15.9^{+9.1}_{-7.8}$	...	...	26^{+26}_{-20}	...	$22.3^{+1.1}_{-9.4}$
Si XIV Lyα	6.185	$5.0^{+1.3}_{-1.2}$	$9.8^{+4.6}_{-3.8}$	$18^{+6.4}_{-5.7}$	...		46^{+22}_{-18}	...	$13^{+5.1}_{-4.5}$
Si XIII *r*	6.648	$1.3^{+0.8}_{-0.8}$	...	< 15	...	...	...	< 6.9	< 3.8
Si XIII *i*	6.686	$1.1^{+0.8}_{-0.7}$	...	< 3.2	...	...	...	< 4.1	$2.5^{+5.0}_{-0.6}$ [b]
Si XIII *f*	6.741	$3.9^{+1.1}_{-1.0}$	...	$9.0^{+4.2}_{-3.5}$	...	...	< 13	$5.9^{+4.2}_{-3.7}$ [b]	$4.7^{+3.8}_{-3.0}$
Mg XII Lyα	8.423	$4.3^{+1.3}_{-1.1}$	$3.4^{+2.2}_{-1.9}$	$8.9^{+4.8}_{-4.1}$	...	...	...	...	$4.5^{+3.7}_{-3.1}$
Mg XI *r*	9.169	$1.9^{+1.0}_{-0.9}$	$2.1^{+2.3}_{-2.0}$	< 4.3	...	...	...	< 8.8	< 3.0
Mg XI *i*	9.229	$5.7^{+1.5}_{-1.4}$	$6.5^{+3.3}_{-2.9}$	$5.0^{+5.1}_{-4.2}$	...	...	< 14	12^{+10}_{-8}	$6.6^{+5.1}_{-4.4}$
Mg XI *f*	9.314	$2.5^{+1.1}_{-1.0}$	$3.8^{+2.4}_{-2.3}$	< 4.4	...	...	...	< 6.5	$4.7^{+2.3}_{-3.1}$ [b]
Ne X Lyβ	10.239	$2.8^{+1.2}_{-1.1}$	...	...	...	...	...	...	...
Ne X Lyα	12.135	$13^{+3.0}_{-2.6}$	$21.8^{+7.8}_{-6.7}$	27^{+12}_{-10}	...	...	...	42^{+25}_{-20}	30^{+14}_{-12}
Ne IX *r*	13.447	< 4.6	$1.6^{+5.8}_{-1.6}$	< 11	...	...	$33^{+65}_{-0.5}$	< 26	$8.2^{+16}_{-1.4}$ [b]
Ne IX *i*	13.551	$30^{+5.4}_{-4.7}$	$29^{+10}_{-8.8}$	53^{+22}_{-14}	...	...	44^{+34}_{-26}	40^{+30}_{-22}	21^{+14}_{-11}
Ne IX *f*	13.699	$2.5^{+2.7}_{-1.7}$	$4.5^{+5.9}_{-4.3}$	< 9.5	...	...	< 63	< 36	< 21
O VIII Lyβ	16.005	$2.6^{+2.8}_{-2.0}$	...	...	...	...	...	...	...
O VIII Lyα	18.968	42^{+14}_{-11}	53^{+29}_{-20}	32^{+32}_{-21}	...	...	$2.4^{+1.4}_{-1.1}$	107^{+91}_{-62}	82^{+52}_{-39}
O VII *r*	21.602	15^{+16}_{-13}	$3.8^{+17}_{-3.7}$	< 27	...	...	...	< 79	< 82
O VII *i*	21.800	148^{+37}_{-32}	195.4^{+74}_{-60}	431^{+150}_{-13}	...	...	< 210	339^{+247}_{-175}	149^{+107}_{-76}
O VII *f*	22.101	14^{+16}_{-11}	< 26	< 20	...	...	...	< 106	< 45
N VII Lyα	24.781	89^{+29}_{-24}	52^{+44}_{-30}	80^{+91}_{-50}	...	...	125^{+206}_{-108}	...	79^{+95}_{-58}
N VI *i*	29.080	133^{+112}_{-112}	< 214	< 685	...	...	...	...	...

Note.
[a] Flux is in the units of 10^{-5} photons s^{-1} cm^{-2}.
[b] 67% confidence level.

that fluorescence line fluxes are measured after the application of continuum column densities. Intrinsic column densities are much higher in the main-on low states and these measurements indicate less Fe K fluorescence than we would expect from the observed optical depth in the K edge.

4. LINE EMISSIVITY DISTRIBUTIONS

We also observe highly ionized emission lines in all observations. The existence of radiative recombination continua (RRCs) demonstrates that we observe a photoionization-dominated plasma (Jimenez-Garate et al. 2005), and their strengths are consistent with our measured *G* and *R* ratios where it applies. No absorption features have been detected in any of the spectra. In order to determine the ionization balance in each of the observed phases, we also apply the photoionization code XSTAR to model all the lines.

4.1. General Line Fits

Using the results from the continuum analysis, we first fit all these lines with Gaussian functions. The discrete emission lines of H-like and He-like ions are significantly detected at all phases except during the high states of main-on phase (OBSIDs 4585 and 6149, for details see Table 5). For the weak lines, we fix the line width to 0.001 Å and keep the line centroid at the theoretical value. For the strong lines, we fit all line components. As it turns out, the line centroids remain with a 90% error within the instrumental resolution, and line width are less than a few tens of mÅ. No Doppler shifts have been detected.

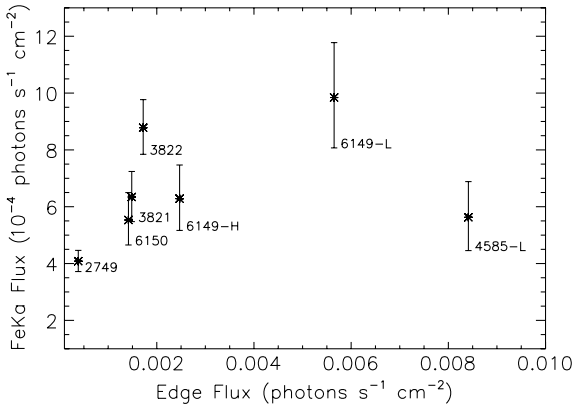

Figure 6. Fe edge flux vs. Fe K_α.

The left panel of Figure 7 shows the results of the line fits for all observations (each color represents one individual observation). Under the assumption that the illuminating source does not vary in between phases, we also fit the lines simultaneously for all observations to obtain average properties. The results of the simultaneous fits are shown in the right panel of Figure 7. This average flux distribution gives us more significance for the parameters of the photoionization modeling.

4.2. Helium-like Triplets

Triplet lines from He-like ions are widely used to provide diagnostics (Porquet et al. 2001) for the electron density and temperature, and also the determination of ionization processes (photoionization or collisional ionization). He-like lines consist

Table 6
He-like Lines[a] for Her X-1

Ion	Si XIII	Mg XI	Ne IX	O VII
		ID 2749		
$G = \frac{(f+i)}{r}$	$4.3^{+6.6}_{-1.9}$	$4.1^{+3.9}_{-1.6}$	> 7.1	$13^{+37}_{-7.4}$
$R = \frac{f}{i}$	$3.9^{+7.7}_{-1.8}$	$0.5^{+0.3}_{-0.2}$	$0.09^{+0.09}_{-0.07}$	$0.6^{+0.1}_{-0.1}$
Cash dof	36/37	17/16	11/15	10/17
		ID 3821		
$G = \frac{(f+i)}{r}$	...	$4.2^{+120}_{-2.5}$	> 3.9	> 2.5
$R = \frac{f}{i}$	...	$0.7^{+0.9}_{-0.5}$	< 0.4	< 0.5
Cash dof	...	18/23	48/17	51/18
		ID 3822		
$G = \frac{(f+i)}{r}$	> 3.1	> 0.5	> 2.7	> 2.4
$R = \frac{f}{i}$	> 1.8	< 1.4	< 0.3	< 0.3
Cash dof	31/40	5.2/13	12/12	39/16
		ID 4585-L		
$G = \frac{(f+i)}{r}$	...	...	$2.9^{+8.4}_{-1.6}$	...
$R = \frac{f}{i}$	...	...	< 1.3	...
Cash dof	...	...	37/22	...
		ID 6149-L		
$G = \frac{(f+i)}{r}$	> 0.1	> 0.7	> 4.2	$3.8^{+3.9}_{-2.6}$
$R = \frac{f}{i}$	> 0.2	< 1.3	< 0.9	$0.3^{+0.4}_{-0.2}$ *b*
Cash dof	39/41	16/21	15/19	14/11
		ID 6150		
$G = \frac{(f+i)}{r}$	> 1.0	> 1.8	> 1.6	$5.0^{+32}_{-3.0}$ [b]
$R = \frac{f}{i}$	$1.5^{+3.6}_{-0.8}$ [b]	$0.7^{+1.7}_{-0.6}$	$0.3^{+0.5}_{-0.3}$ [b]	< 0.5
Cash dof	42/31	1.9/12	27/26	11/10

Notes.
[a] The line center is fixed at the theoretical value and the line width is fixed as 0.001 Å.
[b] At 67% confidence level.

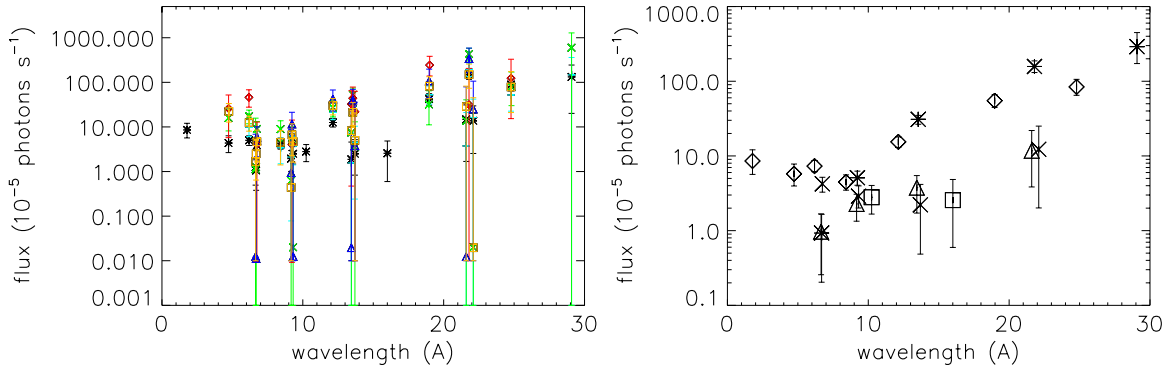

Figure 7. Left: the detectable lines for all observations (ID 2749-black, ID 3821-cyan, ID 3822-green, ID 4585-L-red, ID 6149-L-blue, ID 6150-gold); right: the average detectable lines (Lyα, diamond; Lyβ, square; resonance, triangle; intercombination, asterisk; forbidden, x).

of a resonance (r), an unresolved intercombination line duplex (i), and a metastable forbidden line (f). The most common triplet diagnostics involve ratios sensitive to plasma density, temperature, as well as ionization state. The flux ratio $G = (i+f)/r$ is sensitive to plasma temperature and ionization states, the flux ratio $R = f/i$ to density. We detected He-like triplet lines in the following states: the low (OBSID 2749), turn-on/off states (OBSIDs 3821, 3822, and 6150), and the main-on low states (OBSIDs 4585 and 6149), although the statistics are poor in the most states. No detection (less than 1σ) is in the main-on high states. The fitted R and G ratios are presented in Table 6.

As claimed in Bautista & Kallman (2000), the ionization mechanism of the observed plasma must be established before the analysis of the line diagnostics, or these triplet line diagnostics are misleading. RRC are typical signatures of photoionization-dominated plasma. By fitting with the "redge"

function in XSPEC, the electron temperature measured from the Ne IX, O VIII, O VII, and N VII RRC is in the range of several to tens of eVs, corresponding to 10^4 to 10^6 K. The broad ranged ionization states and weak RRC features thus indicate multiple temperatures of the plasma.

In the HETG wavelength range, lines from $n = 3$ levels ($^3P - {}^1S$) provide direct evidence of the photoionized nature of a plasma (Bautista & Kallman 2000). The relative strengths of these lines to the r lines are different in coronal and photoionization plasmas. However, these lines have generally poor statistics in these observations and the r line is very weak as well.

Most of the triplet lines we detected show strong intercombination lines, which could result in two ways. Both strong radiation fields (by photoexcitation) and high densities (by collisional excitation) can significantly depopulate the ^3S to ^3P, leading to a strong intercombination line and a weak forbidden line (Porquet et al. 2001). In case of pure photoionized plasmas where collisional excitations occur above the critical density, we determine the density limit based on the R ratio according to the calculations from Porquet & Dubau (2000). R ratios of Mg XI, Ne IX, and O VII (see Table 6) are in the range of 0.0–1.5, indicating densities larger than $\sim 10^{11}$ cm^{-3}, while R ratios of Si XIII indicate densities of less than 10^{14} cm^{-3}.

Most of the G ratios from the Si XIII, Mg XI, Ne IX, and O VII triplets suffer from poor statistics and are given with 3σ lower limits. The best detection is Mg XI in the low state ID 2749. Its value of $4.1^{+3.9}_{-1.6}$ is consistent with the value from Jimenez-Garate et al. (2005). The best value indicates an electron temperature range spanning roughly from 2×10^6 K to 5×10^6 K (Porquet & Dubau 2000).

5. EMISSION MEASUREMENT ANALYSIS

The differential emission measure (DEM) analysis is used for modeling the ionization balance in X-ray binaries (e.g., Sako et al. 1999; Jimenez et al. 2005; schulz et al. 2008). Assuming the emission spectrum is dominated by recombination, the line luminosity can be expressed as

$$L_{\rm ul} = \int n_e n_{z,i+1} E_{\rm ul} \alpha^{\rm eff} dV = \frac{A_Z n_H}{n_e} \int f_{i+1} E_{\rm ul} \alpha^{\rm eff} d({\rm EM}), \quad (1)$$

where $A_Z = n_Z/n_H$ is the relative element abundance to hydrogen, f_{i+1} is the ionic fraction of the recombining ion, $E_{\rm ul}$ is the transition energy, and $\alpha^{\rm eff}$ is the effective recombination rate which causes the line emission through the transition $u \rightarrow l$, $d({\rm EM}) = n_e^2 dV$, and $n_{z,i+1} = A_Z n_H f_{i+1}$. Given the detections of the line luminosities, EM distributions can be predicted with XSTAR. Note, $\alpha^{\rm eff}$ includes the contributions from the radiative and di-electronic recombination, cascading effect as well as the possible collisional excitation. As claimed in Porquet & Dubau (2000), the cascading contribution is significant at low temperatures.

We also directly derive EMs from the line formation in the XSTAR model without any other assumptions, which automatically accounts for the cascading effect

$$L_{\rm ul} = \int n_u^{'} A_Z n_H / n_e^2 E_{\rm ul} A_{\rm ul} d({\rm EM}), \quad (2)$$

where $n_u^{'} = n_u/n_Z$ is the upper energy level population of the ion relative to the element abundance, which is easy to be extracted from XSTAR. $A_{\rm ul}$ is the spontaneous transition rate.

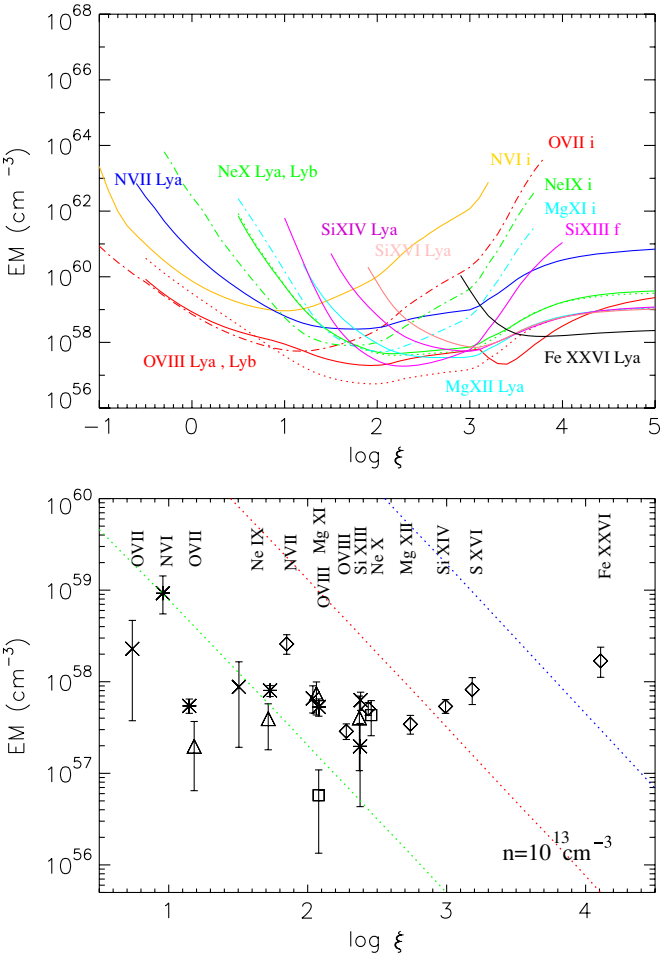

Figure 8. Upper panel: EM curves for the strong lines based on the XSTAR photoionization grid. Lower panel: symbols—the average EM for all detectable lines; symbol are the same as Figure 7. Lines—calculation of EM in dependence of ionization parameter for a static corona for two different luminosities, $L = 10^{38}$ erg s^{-1} (blue-dash), $L = 10^{37}$ erg s^{-1} (red-dash), and $L = 10^{36}$ erg s^{-1} (green-dash). See the text for details.

We first construct a reasonable grid for the photoionization plasma applicable to Her X-1. The fixed power-law photon index of 1.068 is determined from the continuum fitting and the column density is low ($N_H \sim 10^{17}$ cm^{-2}). The grid assumes three densities ($n_e = 10^{11}, 10^{13}, 10^{16}$ cm^{-3}), the ionization parameter ($\log \xi$) spans from -0.1 to 5.0 with 0.1 interval steps. All calculations assume a solar abundance. For each of $\log \xi$, we then derive a corresponding EM according to the observational flux.

The $n_e = 10^{13}$ cm^{-3} photoionization XSTAR grid, for example, then determines the EM functions for the strong lines in the upper panels of Figure 8. We find that the pure radiative recombination rate as a first approximation to the effective recombination rate is not a good measure since the difference to the one including cascading effect amounts to $\sim$2.5 times for the O VII resonance line at $\log \xi \sim 1$. The cascading effect in this set of XSTAR modeling thus cannot be neglected.

In order to get an average EM for each line, the $\log \xi$ has to be weighted by $n_u A_{\rm ul}$, which is in units of photons cm^3 s^{-1}. Specifically, we adopt the average ionization parameter $\langle \log \xi \rangle = \frac{\sum \log \xi n_u A_{\rm ul}}{\sum n_u A_{\rm ul}}$. The average EM is chosen at that average ionization parameter. We got the average EM for all lines at the weighted $\log \xi$ in the lower panel of Figure 8.

It is noted that except for the N Lyα line, all the resonance lines show a common trend in the EM distribution. Nitrogen clearly appears overabundant, which is consistent with the analysis of ID 2749 from Jimenez-Garate et al. (2005). They argued that the CNO process can produce an overabundance of nitrogen and depletion of carbon and oxygen for 2–12 $M_{\odot}$ stars (Jimenez-Garate et al. 2005, and reference therein).

The EMs of the O VII and Ne IX triplet lines are much more complex. We find that the EMs of the intercombination and forbidden lines are well above those of the resonance lines. The reason for this likely lies in the fact that we use one density value for a single grid. In our case, we chose a density that closely matches Mg XI and higher elements, which is higher than what O VII and Ne IX require. The EMs of Mg XI and Si XIII are well consistent with each other due to the appropriate density, and the average values are about 6×10^{57} cm^{-3} and 4×10^{57} cm^{-3}, respectively. The S^3 levels in O VII and Ne IX are depopulated in excess, which results in higher emissivities (therefore the higher EM) of the intercombination lines. The calculations show that we get fairly matching EMs for O VII at a density of $\sim 1 \times 10^{12}$ cm^{-3}. The forbidden line EM never fully match which is likely a consequence that we seem to observe higher fluxes than predicted from the emissivities.

Another effect we observe for the O VII and Ne IX triplets is that their weighted $\log \xi$ are slightly different. The weighted $\log \xi$ of the forbidden lines are much lower than that of the intercombination and resonance lines, particularly for O VII. We think this is due to the different atomic transition processes accounted for in XSTAR with respect to these triplet lines. There are three atomic processes which can excite the He-like ion in a photoionized plasma: (1) direct collisional excitation from the ground state as seen in the collisional plasmas; (2) either radiative or dielectronic recombination from H-like ions; and (3) K shell photoionization of Li-like ions. Process (1) excites the various upper levels, mainly $1s2p(1P)$, resulting in the resonance line. Since it is generated from the ground state, it traces the He-like ion abundance. Process (2) excites the $1s2p(3P)$ more than the $1s2s(3S)$ and $1s2p(1P)$. The radiative recombination tends to populate the upper levels according to 3:1:1, which however is modified by the $3P$ branching to 2.1:1.9:1.0. This process involves the H-like ion, so it shifts the emissivity curves for the intercombination line to the higher ξ. Therefore, the weighted ξ of the intercombination line is higher than that of the resonance line. Process (3) only excites the $1s2s(3S)$. It comes from a Li-like ion, tracing the abundance of the O VI ion, and shifting the forbidden lines to the lower ξ. Therefore, the weighted ξ of the forbidden line is lower than that of the resonance line.

We also note that in the current XSTAR version, K shell photoionization of the Li-like ion for Ne IX has not been updated and may not be as accurate as the other ions. For O and Fe, the XSTAR K shell photoionization cross sections from Li-like ions are taken from *R*-matrix calculations (Garcia et al. 2005; Bautista et al. 2003), and so are likely to be an accurate description of the distribution of final states in the He-like ions. For other elements, the K shell cross sections are taken from central potential calculations (Verner & Yakovlev 1995) and assume that all the final state ions are produced in their ground state. Thus, they do not account for the production of He-like ions in the $1s2s(3S)$ state. Therefore, the atomic process (3) cannot fully account for the lower ξ for Ne IX at its appropriate density of 3×10^{12} cm^{-3}. We speculate that it is a temperature effect that causes the different $\log \xi$'s for Ne IX. The resonance and intercombination lines usually favor higher temperatures leading to higher ionization parameter estimates. Last, but not the least, we should emphasize that assigning a single ξ to the O VII and Ne IX triplets is not ideal. Future approaches should feature deconvolution techniques to trace different ion abundances once better physical models become available for Her X-1.

As argued by Schulz et al. (2008; Figure 5), for Her X-1 with a neutron star about 1.5 ± 0.3 $M_{\odot}$, $\frac{d\mathrm{EM}}{d\xi} \sim 2.0 \times 10^{65} \xi^{-3} L_{38}^2 R_{i7}^{-3/2} T_4^{1/2}$ for a static corona. However, here we use the more accurate numerical integration of Equation (2) in Schulz et al. (2008), and these are shown as the dash lines in Figure 8 for a single-stream treatment of the transfer of the X-ray luminosity of $L = 10^{38}$ (blue-dash), 10^{37} (red-dash), and 10^{36} (green-dash) erg s^{-1} for a disk extending from $10^{8.3}$ to 10^{11} cm. Note, we set the inner disk radius to the corotation radius: $r_{\mathrm{co}} = (GMP_{\mathrm{spin}}^2/4\pi^2)^{1/3} \sim 2 \times 10^8$ cm, which is also about the magnetospheric radius. This shows that at $\log \xi \sim 4.1$, an EM (1.7×10^{58} cm^{-3} for Fe XXVI, for example) that we infer from the observations can only be produced by an ADC if the source luminosity is well above 10^{38} erg s^{-1}. However, the luminosity we infer from the continuum fits is almost an order of magnitude lower. Several other lines fluxes (Si XIII and S XVI) exceed a source luminosity of 10^{37} erg s^{-1} although they are only slightly higher than the predictions of the static corona. Similar for Cir X-1, the true luminosity intrinsic to the source may be much greater than what we observe, which might be due to the obscuration or collimation of the radiation into a direction away from our line of sight.

6. DISCUSSION

Energy spectra early on indicated a dominant presence of photoelectric absorption and electron scattering during most states in Her X-1 (Becker et al. 1977; Davison & Fabian 1977; Pravdo et al. 1977; Parmar et al. 1980). Column densities deduced from broadband low-resolution spectrometers range from $<7 \times 10^{21}$ cm^{-2} in the on-state to 3×10^{23} cm^{-2} in dips. Thus, the Galactic column of about 10^{18} cm^{-2} is negligible in comparison to those intrinsic values between 10^{21} and 10^{23} cm^{-2}. With the availability of increased spectral resolution and sensitivity, more detailed information about the nature of the spectral continuum emerged at specific orbital and superorbital phases. Rocket flights in the mid-1970s discovered significant soft emission coinciding with high flux periods and low columns (Shulman et al. 1975; Catura & Acton 1975) which has later been confirmed as soft ($\sim$0.1 keV) blackbody emission by *Einstein* (McCray et al. 1982) and *BeppoSAX* (Oosterbroek et al. 1997). *XMM-Newton* observed Her X-1 at three superorbital phases, near main-on, short-on, and low state, and modeled the continuum with a partial covering absorption model which included the power law and as well as the soft blackbody spectrum. Extreme changes in partial column were observed, ranging from the low interstellar value near the main-on to 6×10^{23} cm^{-2} for the power-law component in the low state, with significant changes of the ratio of the covering fractions between states (Ramsay et al. 2002). These latter authors also find that by keeping the power-law index fixed to 0.85, the fits above 2 keV also matched consistently well. While closely monitoring the turn-on phase with *RXTE* and expanding the energy range to 17 keV, Kuster et al. (2005) could further develop the partial covering model above 2 keV involving a fixed power-law index of 1.068 and an evo-

lution of cold photoelectric absorption and Thomson electron scattering.

This partial covering model involving a soft blackbody and a cutoff power law with fixed index at 1.068 and a cutoff at 21.5 keV works well for all HETG observations between about 0.3 and 8 keV. The blackbody, with an average temperature of 114 ± 32 eV, is required at all phases including the highly absorbed low states. The emission radius amounts to somewhat less than 100 km, which is smaller than the one deduced from the *XMM-Newton* observations (Ramsay et al. 2002), but still large enough to favor an association with the inner disk over the neutron star surface. Column densities appeared consistently high and highly variable—varying from 9.3×10^{22} cm^{-2} during the Main-high state to 3.2×10^{23} cm^{-2} during the Main-low state. The fact that we observe sizeable absorption even during the high flux states is remarkable, specifically since *XMM-Newton* observations do not find significant amounts during the high flux states that they viewed (Ramsay et al. 2002). However, our observed absorption is consistent with the findings by Kuster et al. (2005) during their monitoring of the turn-on. The *Chandra* HETG archive observations cover several different orbital and superorbital phases of Her X-1. The fact that we obtain good fits with a nearly fixed continuum shape (frozen power-law slope and reasonably constant blackbody temperature) and minimal observable changes in the line-derived ionization balance, while we see large changes in the column, leads us to the conclusion that most if not all changes in X-ray flux are due to absorption, obscuration, and scattering effects relating to the line-of-sight geometry.

Strong line fluorescence is a good indicator of large amounts of cool circumstellar material present in close vicinity of the central X-ray source. Iron line fluorescence was discovered in Her X-1 by Pravdo et al. (1977) and not only is it present at all superorbital phases (Kahabka 1995) but there are indications that it varies over the 1.24 s pulse phase and the 35 day cycle (Choi et al. 1994). We also resolve Fe line fluorescence in most observations, but only once during the Main state. This shows that fluorescence is not detectable at all time. Furthermore, it was not detected during Main-high where the X-ray flux was highest. This is actually consistent with another finding of our study. Figure 6 shows a positive correlation of the Fe K_α line flux with the source flux, but some anticorrelation with equivalent width. The non-detection of the line during Main-high is equivalent to a non-detection of any equivalent width, which fits the same trend. The anticorrelation resembles the "Baldwin effect" which was originally based on a decrease of C IV eWs with respect to UV luminosity in the AGN (Baldwin 1977). Its physical basis is likely a progressing ionization of cold to warm material columns with increasing luminosity (Nayakshin 2000). Similar trends have been observed in *EXOSAT* and *Chandra* data of X-ray binaries (Gottwald & White 1991; J. M. Torrejón et al. 2009, in preparation). The *XMM-Newton* observations seem to follow this trend as well, but with a major difference that there a broad line was observed with a line centroid shifted toward higher ion states (Ramsay et al. 2002). This is an important result because it shows that if we associate the line fluorescence with cool circum-disk material, the outer disk is either not fully responsible for all the absorption and obscuration observed or the X-ray source itself is changing. In conjunction with the above conclusion that the unabsorbed spectral shape remains more or less constant throughout all the flux changes, any intrinsic changes to the source are solely due to changes in the normalization of the spectrum. We observe Fe K_α line broadenings with velocities between 600 and 2000 km s^{-1} consistent with the *XMM-Newton* measurements, however, we clearly do not observe any significant line shifts. Given the lack of energy shifts, the line broadening is likely of dynamic origin and not associated with either gravitational effects or emission from highly ionized Fe states, as might be expected from the very innermost regions of the disk. A major contribution of the optically thick part of the disk to the line fluorescence seems unlikely because the line properties seem not well correlated with orbital and superorbital phases. Detailed geometrical and optical modeling is necessary, however, to arrive at a consistent picture for the source of this fluorescent emission. At this point, we favor the view that dense cool material is scattered within the corona, i.e., over radii $\gtrsim 10^9$ cm, consistent with the measured line widths.

The possible increasing presence of warm material at higher observed source fluxes may have another consequence. We observe ratios of the Fe K_β over Fe K_α line fluxes which are only near the equilibrium value of 0.13 in the low state and in the turn-on from a low state. In all the other states the ratio is substantially larger, although the corresponding error bar is larger too. One effect we have to consider is that the Fe K_β is relatively weak and blended on top of the Fe K edge. At the higher continua, contrast is decreased and the line flux may be overestimated. Although there is no direct indication of the existence of warm columns other than through the Baldwin effect, part of the high line ratios could be due to blends with unresolved warm transitions.

The main goal of this study is to investigate the line emissivity distributions at various orbital and superorbital phases in Her X-1. In three *XMM-Newton* Reflection Grating Spectrometer (RGS) observations, Jimenez-Garate et al. (2002) covered the low, short-on, and main state. In those observations, the low and short-on flux states produced emission lines from carbon to neon and produced CNO abundances and ADC properties. They also reported an absence of ADC line emission during the main state. An extended ADC was identified in the Her X-1 low state by Jimenez-Garate et al. (2005) using *Chandra* HETG spectra. Our study is an expansion of this study. We detect ADC line emission in the low, the turn-on, and in the main-dip and main-low states. We do not detect lines emission during the main-high state consistent with the findings by Jimenez-Garate et al. (2002). Figure 7 plots all the unabsorbed line fluxes we detected at these states. The flux distribution indicates that the measured ADC lines are likely part of a common EM distribution. Line fluxes vary within a factor of 2 or 3 between states, in which continuum fluxes changes by over an order of magnitude. This leads us to conclude that most changes in the line flux are due to some residual obscuration rather than physical changes of the line emitting region. This is consistent with the above conclusions. It also means that neither the central source nor the ADC emissivities are changing with orbital and superorbital phase.

We therefore calculate an average emissivity distribution from all the observations. This resulting distribution is very similar to the one deduced by Jimenez-Garate et al. (2005). We also find that nitrogen is generally overabundant, which Jimenez-Garate et al. explain in conjunction with the observed carbon depletion in the RGS observations (Jimenez-Garate et al. 2002) and HZ Her's CNO cycle. From the *R* ratios as well as the EM distribution, we infer an ADC density of 1×10^{13} cm^{-3} for Mg XI. From EM adjustments of Ne IX and O VII, we also deduce densities of 3×10^{12} cm^{-3} and 1×10^{12} cm^{-3}, respectively.

Lower densities at lower Z elements are not unusual because their ionization regimes likely involve wider ranges of radii and ionization parameters. The size of the accretion disk is thought to be a few times 10^{11} cm (Cheng et al. 1995), which puts a lower limit to Doppler broadening to be observed in the lines. There is likely a contribution from UV flux locally to the disk which also affects the R value. Significant UV flux would imply that our inferred densities are the upper limits. In case of the Si XIII triplet, we observe a large R ratio which neither the UV nor the collisional transitions can explain. For this ion, the implied density is then a valid upper limit. Our observed line velocities range between 200 and 800 km s^{-1}, which assuming an orbital inclination of 81 deg (Howarth & Wilson 1983) results in ADC radii between 2×10^{10} cm $\lesssim r \lesssim 3 \times 10^{11}$ cm. With respect to the findings by Jimenez-Garate et al. (2005), this is very similar except for a smaller inner radius. This is because we find significantly higher velocities at higher flux states. These radii are consistent with ADCs found sources such as 4U 1822-37 (Cottam et al. 2001), 2S 0921-63 (Kallman et al. 2003), and Cir X-1 (Schulz et al. 2008). These radii are significantly larger than the ones found recently in the Z-source Cyg X-2 (Schulz et al. 2009), which features much higher source luminosities and Doppler line velocities.

We also tested how consistent our observed line emissivities are with respect to the observed source luminosity and a static ADC. Using the model calculations presented by Schulz et al. (2008), we computed EMs as a function of ionization parameters for various source luminosities. While most low-energy lines can be well explained by the observed source luminosity of 5×10^{37} erg s^{-1}, the observed H-like lines of S XVI and Fe XXVI are not explained by such a flux. Such deficiencies, i.e., significant highly ionized lines for a moderate flux, have been found in ADCs of 4U 1822-37 (Cottam et al. 2001), Cir X-1 (Schulz et al. 2008), and here for Her X-1. Further ADC modeling, with a detailed focus on heating budgets, is necessary to find an explanation for these H-like lines. The discrepancies from simple models, however, may be too high to be addressed by simply modifying the static corona model. More likely candidates may need to invoke additional sources of energy, such as magnetic field activities, to explain these results.

We thank Rüdiger Staubert for his help with the ephemeris, and Mike Noble for his help with running the XSTAR models. We gratefully acknowledge the financial support of *Chandra X-Ray Observatory* theory grant TM8-9005X.

REFERENCES

Baldwin, J. A. 1977, ApJ, 214, 679
Bautista, M. A., & Kallman, T. R. 2000, ApJ, 544, 581
Bautista, M. A., Mendoza, C., Kallman, T. R., & Palmeri, P. 2003, A&A, 403, 339
Becker, R. H., Boldt, E. A., Holt, S. S., Pravdo, S. H., Rothschild, R. E., Serlemitsos, P. J., Smith, B. W., & Swank, J. H. 1977, ApJ, 214, 879
Boroson, B., Dil Vrtilek, S., Raymond, J. C., & Still, M. 2007, ApJ, 667, 1087
Brandt, W. N., et al. 1996, MNRAS, 283, 1071
Canizares, C. R., et al. 2005, PASP, 117, 1144
Catura, R. C., & Acton, L. W. 1975, ApJ, 202, L5
Cheng, F. H., Vrtilek, S. D., & Raymond, J. C. 1995, ApJ, 452, 825
Choi, C. S., Nagase, F., Makino, F., Dotani, T., Kitamoto, S., & Takahama, S. 1994, ApJ, 437, 449
Cottam, J., Sako, M., Kahn, S. M., Paerels, F., & Liedahl, D. A. 2001, ApJ, 557, L101
dal Fiume, D., et al. 1998, A&A, 329, L41
Davison, P. J. N., & Fabian, A. C. 1977, MNRAS, 178, 1
Díaz Trigo, M., Parmar, A. N., Boirin, L., Méndez, M., & Kaastra, J. S. 2006, A&A, 445, 179
Garcia, J., Mendoza, C., Bautista, M. A., Gorczyca, T. W., Kallman, T. R., & Palmeri, P. 2005, ApJS, 158, 68
Gottwald, M., & White, N. E. 1991, in Lecture Notes in Physics ed. A. Treves, G. C. Perola, & L. Stella (Berlin: Springer), 134
Hasinger, G., & van der Klis, M. 1989, A&A, 225, 79
Houck, J. C., & Denicola, L. A. 2000, in ASP Conf. Ser. 216, Astronomical Data Analysis Software and Systems IX, ed. N. Manset, C. Veillet, & D. Crabtree (San Francisco, CA: ASP), 591
Howard, I. R., & Wilson, R. 1983, MNRAS, 204, 1091
Howarth, I. D., & Wilson, B. 1983, MNRAS, 202, 347
Jimenez-Garate, M. A., Hailey, C. J., Herder, J. W., Zane, S., & Ramsay, G. 2002, ApJ, 578, 391
Jimenez-Garate, M. A., Raymond, J. C., Liedahl, D. A., & Hailey, C. J. 2005, ApJ, 625, 931
Jimenez-Garate, M. A., Schulz, N. S., & Marshall, H. L. 2003, ApJ, 590, 432
Jonker, P. G., & van der Klis, M. 2001, ApJ, 553, L43
Kaastra, J. S., & Mewe, R. 1993, A&AS, 97, 443
Kahabka, P. 1995, A&A, 304, 227
Kallman, T. R., Angelini, L., Boroson, B., & Cottam, J. 2003, ApJ, 583, 861
Kallman, T. R., Palmeri, P., Bautista, M. A., Mendoza, C., & Krolik, J. H. 2004, ApJS, 155, 675
Ko, Y. K., & Kallman, T. R. 1994, ApJ, 431, 273
Kuster, M., et al. 2005, A&A, 443, 753
Makishima, K. 1986, in Lecture Notes in Physics 266, The Physics of Accretion onto Compact Objects, ed. K. P. Mason, M. G. Watson, & N. E. White (Berlin: Springer), 249
Maloney, P., & Begelman, M. C. 1997, ApJ, 491, L43
McCray, R. A., Shull, J. M., Boynton, P. E., Deeter, J. E., Holt, S. S., & White, N. E. 1982, ApJ, 262, 301
Middleditch, J., & Nelson, J. 1976, ApJ, 208, 567
Nayakshin, S. 2000, ApJ, 534, 718
Oosterbroek, T., Parmar, A. N., Martin, D. D. E., & Lammers, U. 1997, A&A, 327, 215
Oosterbroek, T., et al. 2001, A&A, 375, 922
Palmeri, P., Mendoza, C., Kallman, T. R., Bautista, M. A., & Meléndez, M. 2003, A&A, 410, 359
Parmar, A. N., Sanford, P. W., & Fabian, A. C. 1980, MNRAS, 192, 311
Porquet, D., & Dubau, J. 2000, A&AS, 143, 495
Porquet, D., Mewe, R., Dubau, J., Raassen, J. J., & Kaastra, J. S. 2001, A&A, 376, 1113
Pravdo, S. H., Becker, R. H., Boldt, E. A., Holt, S. S., Serlemitsos, P. J., & Swank, J. H. 1977, ApJ, 215, L61
Ramsay, G., Zane, S., Jimenez-Garate, M., den Herder, J., & Hailey, C. J. 2002, MNRAS, 337, 1185
Raymond, J. C. 1993, ApJ, 412, 267
Sako, M., Liedahl, D. A., Kahn, S. M., & Paerels, F. 1999, ApJ, 525, 921
Schandl, S., & Mayer, F. 1994, A&A, 289, 149
Schulz, N. S., Hasinger, G., & Trümper, J. 1989, A&A, 225, 48
Schulz, N. S., Huenemoerder, D. P., Ji, L., Nowak, M., Yao, Y., & Canizares, C. R. 2009, ApJ, 692, L80
Schulz, N. S., Kallman, T. E., Galloway, D. K., & Brandt, W. N. 2008, ApJ, 672, 1091
Shulman, S., Friedman, H., Fritz, G., Yentis, D. J., & Henry, R. C. 1975, ApJ, 199, L101
Staubert, R., Shakura, N. I., Postnov, K., Wilms, J., Rothschild, R. E., Coburn, W., Rodina, L., & Klochkov, D. 2007, A&A, 465, L25
Still, M., Quaintrell, H., Roche, P., & Reynolds, A. P. 1997, MNRAS, 292, 52
Tananbaum, H., et al. 1972, ApJ, 174, L143
Truemper, J., Pietsch, W., Reppin, C., Voges, W., Staubert, R., & Kendziorra, E. 1978, ApJ, 219, L105
Verner, D. A., & Yakovlev, D. G. 1995, A&AS, 109, 125
Wilms, J., Allen, A., & McCray, R. 2000, ApJ, 542, 914